Research Square

Preprints are preliminary reports that have not undergone peer review.
They should not be considered conclusive, used to inform clinical practice,
or referenced by the media as validated information.

# Machine-learned potentials link vacancy-dependent copper transport to post-implantation profiles in silicon

**Mingzhu Liu**
Central South University
**Yiwen Su**
Hong Kong Polytechnic University
**Xinzhong Wang**
Hong Kong Polytechnic University
**Jiashu Chen**
jiashu.chen@csu.edu.cn

Central South University

**Article**

**Keywords:** Copper diffusion, Silicon contamination, Deep potential molecular dynamics, Vacancy trapping, Ion implantation

**Posted Date:** October 21st, 2026

**DOI:** https://doi.org/10.21203/rs.3.rs-11223831/v1

**License:** This work is licensed under a Creative Commons Attribution 4.0 International License.
Read Full License

**Additional Declarations:** No competing interests reported.

# Machine-learned potentials link vacancy-dependent copper transport to post-implantation profiles in silicon

Mingzhu Liu,[1,2] Yiwen Su,[3] Xinzhong Wang,[3] Jiashu Chen[1*]
[1] School of Physics, Central South University, Changsha, China
[2] Department of Biomedical Sciences, College of Biology, Hunan University, Changsha, China
[3] Department of Mechanical Engineering, Hong Kong Polytechnic University, Hung Hom, Kowloon, Hong Kong, China

*** Corresponding author:** Jiashu Chen (jiashu.chen@csu.edu.cn)

## Abstract
Copper contamination threatens silicon devices because mobile Cu can form electrically active defects and redistribute during thermal processing. Here we combine DFT-informed implantation simulations, an actively learned deep potential (DP) and large-scale molecular dynamics to connect elementary Cu migration with vacancy-dependent transport and annealed depth profiles. The DP reproduces DFT energies and forces with root-mean-square errors of 3.16–3.71 meV/atom and 35.10–88.30 meV/Å, respectively. Nudged-elastic-band calculations yield an interstitial migration barrier of 0.192 eV, close to the DFT value of 0.185 eV, and capture the energetic preference for Cu occupation of a Si vacancy. Across systems containing eight Cu atoms and 0, 2, 4 or 8 Si vacancies, atom-resolved trajectories reveal competition between mobile interstitial Cu and vacancy-associated Cu. Increasing vacancy number raises the prevalence of locally confined Cu and changes the ensemble-averaged transport behaviour. The vacancy-free system has an apparent activation energy of 0.202 eV, comparable in magnitude to reported experimental values of 0.15–0.18 eV. The combined DFT-MD+DP framework also reproduces the principal features of SIMS profiles before and after annealing. Relative to the MC/BCA+KMC workflow assessed here, it reduces mean-normalized NRMSE by 47–61% across the full profiles, with improvements in both the near-surface region and low-concentration tail. By linking Cu–vacancy interactions to measurable redistribution, this framework offers a route to jointly evaluating implantation-induced defects and annealing conditions when seeking to limit mobile Cu and residual Cu–defect complexes in silicon.

## Keywords
Copper diffusion; Silicon contamination; Deep potential molecular dynamics; Vacancy trapping; Ion implantation

## 1. Introduction

Copper has become the dominant metallization material for advanced integrated circuits because of its low electrical resistivity and superior resistance to electromigration compared with aluminium [1,2]. The development of three-dimensional integration and Cu through-silicon vias has further increased the interfacial area over which Cu-containing structures are brought into close proximity to crystalline silicon [1,3]. This integration creates a persistent reliability concern because Cu can penetrate imperfect diffusion barriers, migrate rapidly through Si and subsequently react with native defects or form Cu-rich precipitates and silicide-related phases [4-7]. Controlling Cu incorporation and redistribution is therefore important for interconnect reliability, wafer processing and the fabrication of Si-based electronic and photovoltaic devices.

Copper is also one of the most common metallic contaminants encountered during Si crystal growth and semiconductor processing [8]. Even at low concentrations, Cu-related defects can introduce electrically active states, promote carrier recombination and increase junction leakage currents [9-13]. Cu precipitation has additionally been correlated with gate-oxide breakdown and the degradation of metal-oxide-semiconductor capacitors [14,15]. Transmission electron microscopy and secondary-ion mass spectrometry measurements have further associated Cu redistribution with structural degradation and increased leakage current in Si p-n junctions [16]. In photovoltaic Si, the influence of Cu depends strongly on its concentration, charge state, precipitation behaviour and the conductivity type of the substrate [17-24]. Some measurements indicate a limited effect of moderate Cu concentrations in p-type Si, whereas n-type material can exhibit substantially greater minority-carrier lifetime degradation [19-24]. These apparently different observations reflect the multiple forms in which Cu can exist in Si, including isolated interstitials, substitutional defects, impurity-defect complexes and extended precipitates.

The unusual mobility of Cu originates from its interstitial diffusion mechanism [4,5,25-28]. Positively charged interstitial Cu preferentially occupies tetrahedral sites and migrates between neighbouring tetrahedral positions through a low-energy region close to the hexagonal interstitial site. The intrinsic migration barrier is approximately 0.18 eV, making Cu one of the fastest diffusing transition-metal impurities in crystalline Si [26,27]. Hybrid-functional calculations have reproduced a comparable barrier of approximately 0.19 eV and shown that the relative stability of interstitial and substitutional Cu depends on charge state and Fermi-level position [29]. Static first-principles calculations have reported barriers of approximately 0.24-0.32 eV [28,30,31], suggesting that lattice relaxation, atomic kinetic energy and finite-temperature dynamics can become important for such a mobile impurity.

Rapid interstitial migration does not, however, imply unrestricted macroscopic diffusion. Interstitial Cu readily interacts with Si vacancies, shallow acceptors, dislocations and implantation-induced damage [32-38]. Emission-channeling measurements show that implanted Cu can occupy near-substitutional configurations displaced towards bond-centred positions, with dissociation energies substantially larger than the intrinsic interstitial migration barrier [33]. First-principles calculations further indicate that capture of interstitial Cu by a pre-existing Si vacancy produces substitutional Cu and releases several electronvolts of energy [32,34,35]. Vacancy-related configurations can therefore act as strong kinetic traps: Cu may migrate rapidly while it remains interstitial but become immobilized after entering a vacancy-associated state.

Subsequent transport is governed by competition between interstitial migration, defect capture, detrapping, Cu-Cu association and precipitation [35-38]. The coexistence of mobile and trapped Cu populations makes an atom-resolved description essential for interpreting ensemble diffusion coefficients.

Experimental methods including secondary-ion mass spectrometry, transient-capacitance measurements, emission channeling and carrier-lifetime measurements have provided important information on Cu depth distributions, diffusivities and lattice locations [3,4,16,23,24,26,33,38]. Nevertheless, these measurements generally probe spatially or temporally averaged observables and cannot directly resolve individual capture and release events. A measured Cu concentration profile may therefore reflect the combined effects of implantation, surface loss, long-range migration, trapping, precipitation and the evolving population of implantation-induced defects. In particular, agreement near the concentration maximum does not necessarily ensure an accurate description of the near-surface region or the low-concentration diffusion tail.

Atomistic calculations complement these measurements by resolving the elementary migration pathways and defect configurations involved. First-principles methods have been used to determine Cu formation energies, charge states, electronic levels, migration barriers and interactions with vacancies and dislocations [12,29-32,34,37,39]. Their computational cost, however, restricts conventional ab initio molecular dynamics to relatively small cells and short trajectories, which are generally insufficient for statistically converged diffusion coefficients or the heterogeneous defect environments generated during implantation and annealing. Classical molecular dynamics provides access to larger systems, and both conventional and reactive force fields have been applied to Cu diffusion and clustering in Si [28,40]. Their accuracy and transferability remain dependent on the assumed functional form and the configurations included during parametrization.

Machine-learned interatomic potentials provide a route across this scae gap by retaining a first-principles description of the local energy landscape while enabling substantially larger and longer atomistic simulations. Active-learning strategies can further reduce training-set redundancy by identifying uncertain configurations for additional first-principles labelling [41]. For ion implantation, DFT-informed full molecular dynamics provides a more complete representation of atom-atom interactions and substrate response than recoil-interaction or binary-collision approximations [42,43]. A recently developed DFT-MD and deep-potential framework has also demonstrated that implantation-induced defects and subsequent defect-mediated diffusion can be treated within a physically consistent atomistic workflow [44,45]. These advances provide the methodological basis for connecting implantation, annealing and impurity transport without prescribing a fixed catalogue of migration events.

Here, we develop an actively learned deep-potential model for Cu-Si and integrate it with DFT-MD implantation simulations to establish a unified description of Cu implantation, defect interactions and post-implantation diffusion. The model reproduces DFT energies with root-mean-square errors of 3.16-3.71 meV/atom and atomic forces with errors of 35.10-88.30 meV/Å. Deep-potential nudged-elastic-band calculations recover an interstitial Cu migration barrier of approximately 0.19 eV and predict an energy gain of approximately 2.5 eV when interstitial Cu is captured by a Si vacancy. Relative to MC/BCA+KMC, the combined DFT-MD+DP framework reduces the mean-normalized NRMSE of the Cu concentration

profiles by 47-61% over the full depth range, by 46-52% in the near-surface region of 0-200 Å and by 53-61% in the 700-900 Å diffusion tail. The calculated profiles also retain approximately 90% of the experimental tail inventory after implantation and annealing. Large-scale simulations of eight Cu atoms in Si containing 0, 2, 4 or 8 vacancies over 600-1400 K reveal long-time Fickian diffusion governed by competition between rapid interstitial migration and vacancy trapping. In vacancy-free Si, the calculated diffusivities differ from the intrinsic experimental reference by a geometric-mean factor of 1.98 and yield an activation energy of 0.202 eV, compared with the experimental value of 0.15 eV. Increasing vacancy concentration suppresses Cu diffusivity and produces increasingly confined and intermittent atomic trajectories. These results connect elementary Cu-defect interactions with implantation-scale redistribution and provide a first-principles-informed framework for predicting Cu contamination and transport in Si.

## 2. Results

### 2.1. Simulation framework

**Figure 1** outlines the multiscale framework linking Cu implantation, annealing-driven redistribution and vacancy-mediated diffusion in Si. Density functional theory molecular dynamics (DFT-MD) provides the implanted configurations, while an actively learned deep potential (DP) enables large-scale simulations of subsequent Cu transport. The DFT-MD simulation setup and computational parameters are detailed in the **Supplementary Information**.

The DP construction workflow is shown in **Fig. 1a**. The initial dataset contains representative interstitial and substitutional Cu configurations, vacancy-containing structures and intermediate configurations sampled along relevant migration pathways. Additional configurational diversity is introduced through cell deformation and random atomic perturbations. These structures are labelled by DFT calculations to provide reference energies and atomic forces. An ensemble of deep neural network potentials is then trained and iteratively refined using the DP-GEN concurrent-learning scheme. During configuration exploration, model disagreement identifies atomic environments that are insufficiently represented in the existing dataset. These candidate structures are subsequently relabelled by DFT and incorporated into the training set until the model uncertainty converges. This iterative training-exploration-labelling procedure, adapted from our previously reported strategy [41,45], concentrates the computational effort on configurations most relevant to Cu migration and Cu-defect interactions.

The implantation stage is illustrated in **Fig. 1b**. DFT-MD explicitly describes the highly non-equilibrium interactions between energetic Cu ions and the Si lattice, generating atomistically resolved implantation structures without assuming a predefined dopant distribution. The resulting configurations provide the initial states for the post-implantation annealing simulations shown in **Fig. 1c**. At this stage, the trained DP model enables DeePMD simulations over substantially larger length and time scales than those accessible to conventional ab initio molecular dynamics, while retaining the accuracy of the underlying DFT reference data within the sampled configurational space.

The depth-dependent Cu profile obtained immediately after implantation is shown in **Fig. 1d**. This profile characterizes the penetration depth, peak position and spatial broadening produced by the

implantation process. **Fig. 1e** shows the corresponding Cu distribution after thermal annealing, revealing the redistribution of implanted Cu through thermally activated diffusion. The calculated profiles are evaluated against secondary-ion mass spectrometry measurements and MC/BCA+KMC predictions, thereby connecting the atomistic simulations with experimentally measurable dopant distributions.

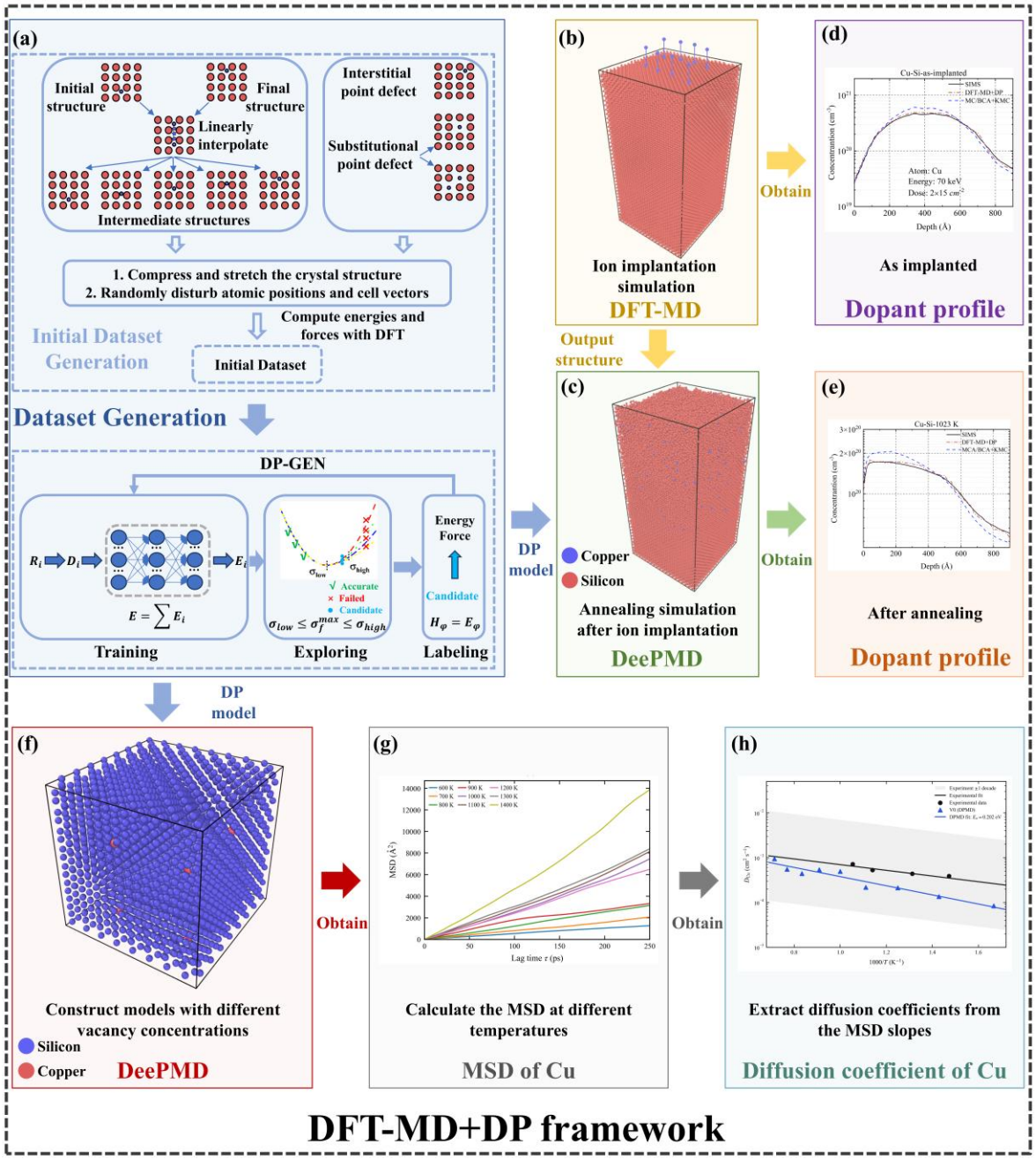



**Fig. 1 | Multiscale DFT–MD and deep-potential framework for Cu implantation and diffusion in Si. a,** Generation of the reference dataset and concurrent-learning workflow used to train the Cu–Si deep-potential (DP) model. Initial structures include interstitial and substitutional point defects and are augmented by structural perturbations; configurations sampled during exploration are selected according to the model deviation and labelled by density functional theory (DFT). **b,c,** Representative atomic

configurations used for DFT molecular-dynamics simulations of Cu implantation and DP molecular-dynamics simulations of post-implantation annealing, respectively. **d,e,** Calculated Cu depth profiles before and after annealing. **f,** Construction of large Si cells containing different numbers of Si vacancies. **g,** Temperature-dependent Cu mean-squared displacement (MSD). **h,** Extraction of Cu diffusion coefficients from the long-time MSD slopes using the Einstein relation.

To isolate the influence of Si vacancies on Cu transport, four diffusion models containing 0, 2, 4 or 8 Si vacancies are constructed, as shown in **Fig. 1f**. Each model contains eight Cu atoms in a 4096-site Si host and is simulated over 600–1400 K. **Fig. 1g** presents the resulting Cu mean-squared displacement (MSD) curves. Cu atoms are tracked individually using their unwrapped coordinates, and the self-MSD is calculated relative to the first frame of the production trajectory. The three-dimensional diffusion coefficient is extracted from the long-time Fickian regime according to $D_{Cu}=1/6\cdot d< r^2(t)>/dt$.

Finally, **Fig. 1h** summarizes the diffusion coefficients obtained from the MSD slopes and their comparison with the experimental Arrhenius relationship. Temperature-dependent diffusion coefficients, activation energies and pre-exponential factors are subsequently determined for the four vacancy models. Together with the individual Cu trajectories, these results provide a direct atomistic description of the competition between rapid interstitial migration and vacancy trapping. Detailed settings for the DFT, active-learning, implantation and DeePMD calculations are provided in the Methods and Supplementary Information.

### 2.2. Accuracy assessment of the DP model

To assess the predictive accuracy of the trained DP model independently of the training procedure, we constructed separate test datasets for the $Si_{64}Cu$, $Si_{63}Cu$ and $Si_{62}Cu_2$ systems. Each test set contains 100 configurations generated using the same physically motivated sampling protocol as the initial dataset, including lattice deformation and random perturbations of the atomic coordinates and cell vectors, but these configurations were not used to optimize the model parameters. The workflow is summarized in Fig. 1a, and the corresponding coordinate files and generation procedures are provided in the Supporting Information.

The DP model was trained by minimizing a composite loss function containing energy and force residuals,

$$L(p_\epsilon, p_f) = \frac{1}{l}\sum_{l}\left(p_\epsilon|E_l-E_l^w|^2+p_f|F_l-F_l^w|^2\right)$$

where $l$ denotes the index of the training data. $E_l$ and $F_l$ represent the reference energy and force, respectively, while $E_l^w$ and $F_l^w$ denote the predicted energy and force, respectively. $p_\epsilon$ and $p_f$ are tunable prefactors [46].

**Fig. 2a** compares the DFT and DP energies for the $Si_{64}Cu$ test configurations. The predictions closely follow the parity line over the sampled energy range, yielding an energy RMSE of 3.16 meV/atom. **Fig 2b** shows the corresponding force comparison. The ***x*-, *y*-** and ***z*-**components cluster around the parity line without an evident directional bias, giving a force RMSE of 35.10 meV/Å. A representative $Si_{64}Cu$

configuration used in this assessment is shown in **Fig. 2c**.

The $Si_{63}Cu$ system introduces a more heterogeneous local environment associated with the Si vacancy. The energy comparison in **Fig. 2d** gives an RMSE of 3.71 meV/atom, while the force components in **Fig. 2e** yield an RMSE of 59.51 meV/Å. The corresponding defect-containing atomic structure is presented in **Fig. 2f**. Despite the increased structural complexity, the close agreement between the DP and DFT values indicates that the model captures the energetic and mechanical responses associated with vacancy-modified Cu environments.

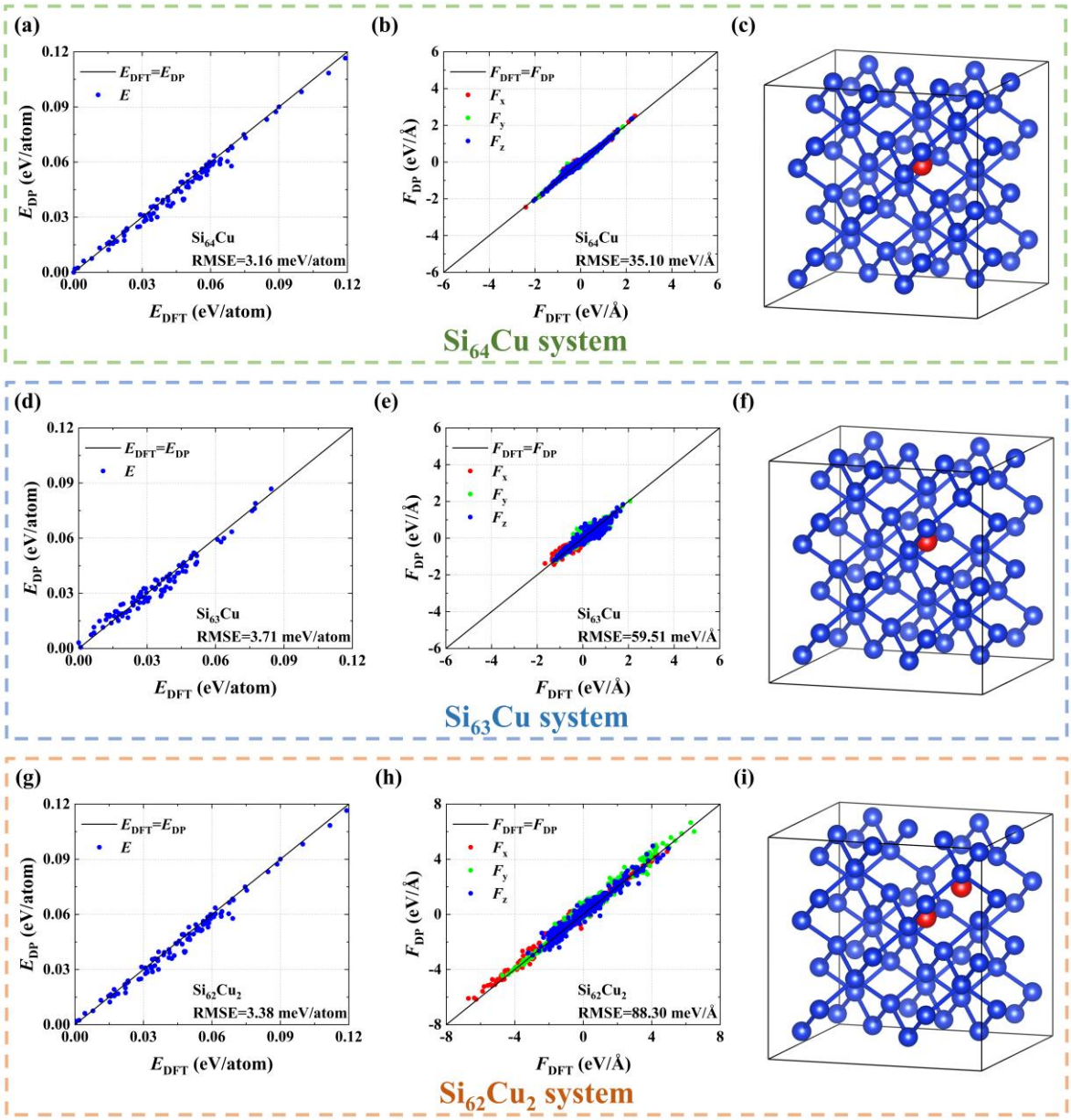



**Fig. 2 | Validation of the Cu–Si deep-potential model against DFT calculations.** Parity plots of atomic energies, Cartesian force components and representative atomic configurations are shown for $Si_{64}Cu$ **(a–c)**, $Si_{63}Cu$ **(d–f)** and $Si_{62}Cu_2$ **(g–i)**. Red, green and blue points represent the *x*-, *y*- and *z*-components of the

atomic forces. Blue and red spheres denote Si and Cu atoms, respectively.

The most chemically and structurally complex test set, $Si_{62}Cu_2$, is evaluated in **Fig. 2g**. It's energy RMSE is 3.38 meV/atom, remaining comparable to those of the other two systems. **Fig. 2h** gives a force RMSE of 88.30 meV/Å, and the representative two-Cu configuration is shown in **Fig. 2i**. The progressive increase in force error from $Si_{64}Cu$ to $Si_{62}Cu_2$ reflects the greater diversity and steeper local energy gradients introduced by Cu-Cu and Cu-vacancy interactions. Nevertheless, the force RMSE remains below 0.1 eV/Å, while the energy errors remain consistently within 4 meV/atom for all three compositions.

**Table 1 |** Test-set root-mean-square errors of the energies and atomic forces predicted by the trained DP model.

| DP system | Energy RMSE (meV/atom) | Force RMSE (meV/Å) |
|---|---|---|
| $Si_{64}Cu$ | 3.16 | 35.10 |
| $Si_{63}Cu$ | 3.71 | 59.51 |
| $Si_{62}Cu_2$ | 3.38 | 88.30 |

Together, the test-set results in **Table 1** demonstrate that the DP model reproduces the DFT potential-energy surface across the principal atomic environments involved in interstitial Cu migration, vacancy trapping and Cu-defect rearrangement. This agreement provides the accuracy required for the subsequent migration-barrier and large-scale diffusion calculations. We further assessed whether the DP model preserves the underlying Si structure by comparing radial distribution functions at 300 K (**Figs. S6** and **S7**). For crystalline Si, the DeePMD curve reproduces the sharp nearest-neighbour peak and the subsequent coordination shells obtained from AIMD (**Fig. S6**). For amorphous Si, it also captures the broadened peaks and reduced long-range order characteristic of the disordered network (**Fig. S7**). The agreement provides a structural check across ordered and disordered Si environments, complementing the energy and force tests. The accuracy of Cu migration and vacancy-capture energetics is assessed separately by the DFT–DP NEB comparisons in **Fig. 3**.

### 2.3. DP prediction of Cu migration and vacancy capture

Interstitial Cu in crystalline Si can occupy tetrahedral ($Cu_i^T$) and hexagonal ($Cu_i^H$) sites [47]. The tetrahedral site is coordinated by four equidistant Si atoms, whereas the hexagonal site is coordinated by six Si atoms and lies midway between neighbouring tetrahedral sites along the ⟨1 1 1⟩ direction. Previous calculations identify $Cu_i^T$ as the more stable interstitial configuration [39]. For visual clarity, tetrahedral interstitial Cu is labelled $Cu_i$ in the main-text **Fig. 3**, while the same configuration is labelled explicitly as $Cu_i^T$ in **Figs. S1–S4**. Throughout this section, $Cu_i$ refers specifically to $Cu_i^T$.

We examined four paths that connect interstitial migration with vacancy capture and Cu-complex formation. The first describes migration between adjacent tetrahedral sites, $Cu_i \rightarrow Cu_i$, whose initial and final configurations are shown in **Fig. S1**. The second describes occupation of a Si vacancy by interstitial Cu, $Cu_i + V_{Si} \rightarrow Cu_s$. F**ig. S2a** shows the initial configuration containing $Cu_i$ and a pre-existing $V_{Si}$, and **Fig. S2b** shows the substitutional Cu product. Previous calculations indicate that vacancy capture is energetically favourable [32,36].

The low migration barrier of $Cu_i$ allows it to move rapidly through the Si lattice and encounter other defects. Depending on the Fermi level, substitutional and interstitial Cu can occur in the oppositely charged states $Cu_s^{2-}$ and $Cu_i^+$, respectively. When these states coexist in n-type Si, electrostatic attraction favours formation of a bound $\langle Cu_s^{2-}, Cu_i^+ \rangle$ pair [29]. Association temporarily removes $Cu_i^+$ from the population available for long-range interstitial migration. Its effect on the measured diffusivity depends on how long the pair persists relative to the time required for migration between sites. Cu transport must therefore be considered in terms of both isolated- $Cu_i$ migration and defect-mediated capture.

To represent the subsequent interaction of a $\langle Cu_s, Cu_i \rangle$ pair with a vacancy, we considered two further paths. In the first, $V_{Si}$ occupies a first-nearest-neighbour site of $Cu_s$ (**Fig. S3a**), and capture of $Cu_i$ produces adjacent substitutional Cu atoms, $\langle Cu_s, Cu_i \rangle$ (**Fig. S3b**). This reaction is written as $\langle Cu_s, Cu_i \rangle + V_{Si} \rightarrow \langle Cu_s, Cu_s \rangle$. In the second path, $V_{Si}$ is initially a second-nearest neighbour of $Cu_s$ (**Fig. S4a**), and the product is $\langle Cu_s, Si, Cu_s \rangle$, in which one Si atom separates the two substitutional Cu atoms (**Fig. S4b**). The corresponding reaction is $\langle Cu_s, Cu_i \rangle + V_{Si} \rightarrow \langle Cu_s, Si, Cu_s \rangle$. Earlier calculations reported energy releases of 2.26 and 2.04 eV for these respective reactions [32]. Together, the two configurations describe distinct ways in which vacancies can incorporate mobile $Cu_i$ into Cu-containing complexes.

We determined the minimum-energy paths using the nudged elastic band (NEB) method [47,48]. This method is widely recognized among researchers who are investigating diffusion mechanisms across various media [49-53]. DFT-based NEB provides reference energies and atomic configurations along each path, but its computational cost limits extensive calculations. NEB calculations with empirical interatomic potentials are less expensive, although their fixed functional forms can limit their description of changing Cu–Si coordination [54,55]. We therefore compared DFT-based NEB with calculations using the trained DP model implemented in LAMMPS [56]. This comparison evaluates the DP model at the higher-energy configurations encountered during migration, in addition to the relaxed initial and final structures.

**Table 2 |** Comparison between the calculation results of migration energy barrier as obtained from DPMD and DFT.

| Diffusion path | Our work (eV) | | Other work (eV) |
|---|---|---|---|
| | DPMD | DFT | |
| $Cu_i \rightarrow Cu_i$ | 0.192 | 0.185 | 0.19 (DFT) [29], 0.18±0.02 (EXP) [57] |
| $Cu_i + V_{Si} \rightarrow Cu_s$ | -2.484 | -2.437 | -2.80 (AIMD) [32], -2.20 (EXP) [57] |
| $Cu_s\text{-}Cu_i + V_{Si} \rightarrow Cu_s\text{-}Cu_s$ | -2.144 | -2.090 | -2.26 (AIMD) [32] |
| $Cu_s\text{-}Cu_i + V_{Si} \rightarrow Cu_s\text{-}Si\text{-}Cu_s$ | -1.767 | -1.811 | -2.04 (AIMD) [32] |

For migration between tetrahedral sites, the DFT and DP energy profiles nearly coincide (**Fig. 3a**). **Fig. 3b** shows the initial $Cu_i$ configuration, and **Fig. 3c** shows the final, equivalent tetrahedral configuration. DFT gives a migration barrier of 0.185 eV, compared with 0.192 eV from DP, a difference of approximately 3.8%. Both values agree with previously reported barriers of 0.190 eV [29] and 0.180 eV [26]. At the saddle point, the mean and maximum positional differences between the DP- and DFT-relaxed atomic structures are 0.020 and 0.032 Å, respectively. The small barrier provides an energetic basis for

rapid migration of isolated $Cu_i$ through crystalline Si. The atomic geometry of this hop is further illustrated in **Fig. S5**.

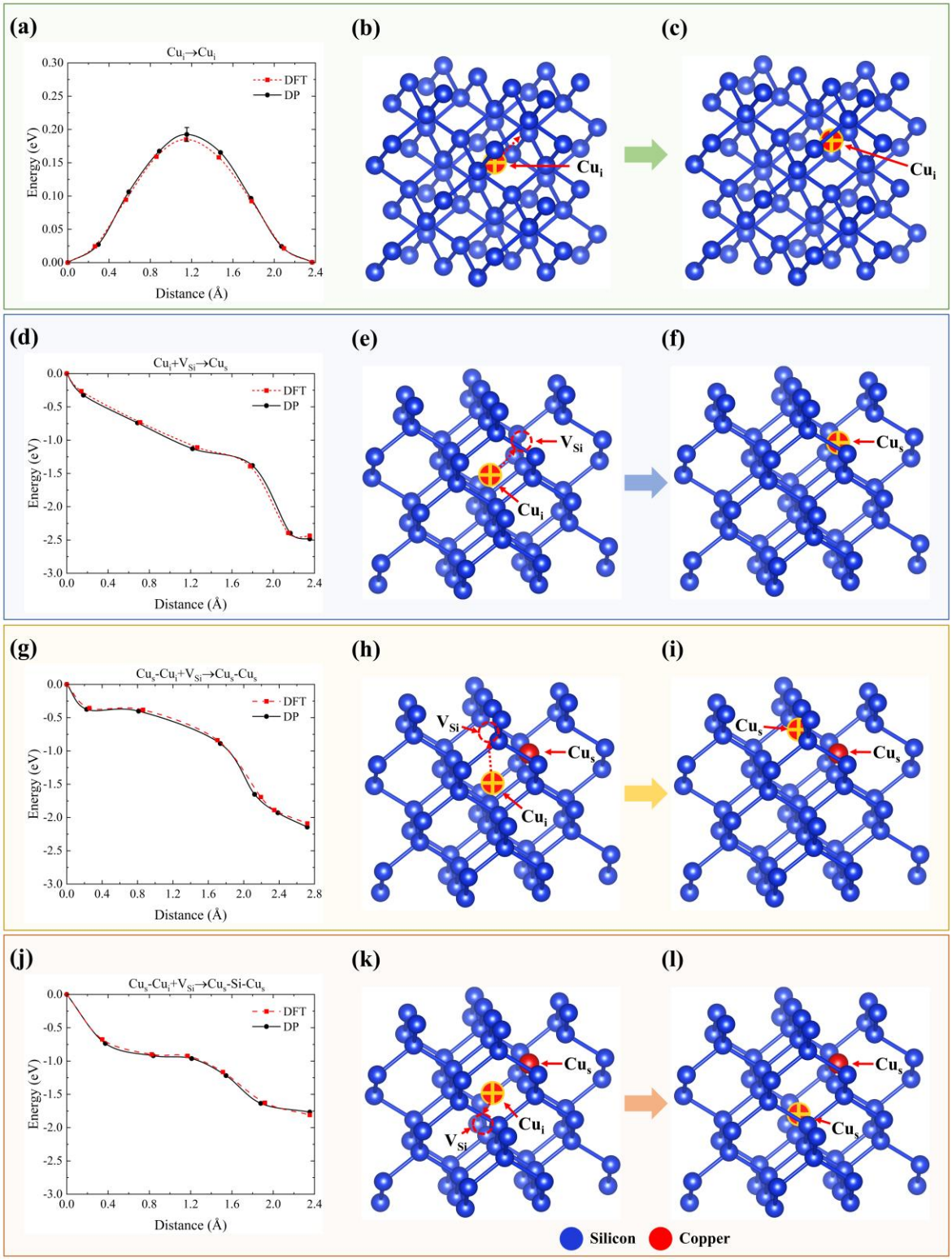


**Fig. 3 | Elementary pathways for interstitial Cu migration and vacancy capture in Si. a–c,** DFT and DP energy profiles and representative structures for the migration of an interstitial Cu atom between neighbouring sites, yielding a migration barrier of approximately 0.19 eV. **d–f,** Capture of an interstitial Cu atom by a Si vacancy to form substitutional Cu, accompanied by an energy reduction of approximately 2.5 eV. **g–i,** Vacancy-assisted rearrangement of a substitutional–interstitial Cu pair into a configuration containing two substitutional Cu atoms. **j–l,** Alternative vacancy-mediated rearrangement producing a $Cu_{Si}$–Si–$Cu_{Si}$ configuration. The left-hand panels show the DFT and DP energy profiles, and the middle and right-hand panels show the corresponding initial and final structures. Blue and red spheres denote Si and Cu atoms; dashed circles and yellow symbols identify the Si-vacancy region and the principal migrating site.

The green arrow traces the displacement of $Cu_i$ between symmetry-equivalent tetrahedral interstitial sites within the Si lattice, complementing the endpoint configurations in **Fig. 3b, c** and the energy profile in **Fig. 3a**. **Fig. S5** thus identifies the spatial path associated with the low migration barrier, whereas the barrier itself is determined from the NEB calculations.

Vacancy capture has a different energy profile. In **Fig. 3d**, the energy decreases as $Cu_i$ moves from the initial $Cu_i$+$V_{Si}$ configuration (**Fig. 3e**) towards the $Cu_s$ product (**Fig. 3f**). On the plotted energy scale, the product lies approximately 2.5 eV below the initial state. The DP curve follows the DFT result through the gradual initial decrease and the sharper decrease near the product. This agreement indicates that the model describes the substantial change in local coordination as Cu moves from an interstitial site into a vacant Si site. The downhill profile also identifies $V_{Si}$ as a strong energetic sink for mobile $Cu_i$.

The two pair-forming reactions provide further tests of Cu–defect interactions. For $\langle Cu_s, Cu_i\rangle$+$V_{Si}$→$\langle Cu_s, Cu_s\rangle$, the energy initially falls, passes through a relatively shallow region and then decreases towards the adjacent substitutional pair (**Fig. 3g**). The corresponding initial and final configurations are shown in **Fig. 3h** and **Fig. 3i**. The alternative path to $\langle Cu_s, Si, Cu_s\rangle$ shows a similar change in slope but reaches a different final energy on its separately referenced profile (**Fig. 3j**); its structures are shown in **Fig. 3k** and **Fig. 3l**. The shoulders in these profiles are consistent with local atomic rearrangement during capture, although the static NEB results alone do not establish long-lived intermediate states. For both reactions, DP reproduces the principal features of the DFT profiles and the energetic stabilization associated with complex formation.

The four paths reveal competing contributions to Cu transport. Isolated $Cu_i$ can migrate readily because of its low barrier, whereas Si vacancies favour its conversion into substitutional Cu or Cu-containing complexes. The agreement between DP and DFT across these distinct local environments, summarized in **Table 2**, supports the use of the trained model in subsequent large-scale DeePMD simulations. Finite-temperature trajectories are then needed to determine how frequently capture and release occur and how strongly they affect the effective Cu diffusivity.

### 2.4. Vacancy-dependent Cu diffusion and heterogeneous trapping in crystalline Si

We investigated Cu transport in a 4,096-site crystalline Si cell containing eight Cu atoms and 0, 2, 4 or 8 Si vacancies. **Fig. 4a, b** shows projected and three-dimensional views, respectively, of the vacancy-free

V0 simulation cell containing 4,096 Si atoms and eight Cu atoms. To examine the effect of Si vacancies, we constructed the corresponding V2, V4 and V8 models by removing 2, 4 and 8 Si atoms from the same lattice and analysed each model at nine temperatures between 600 and 1400 K.

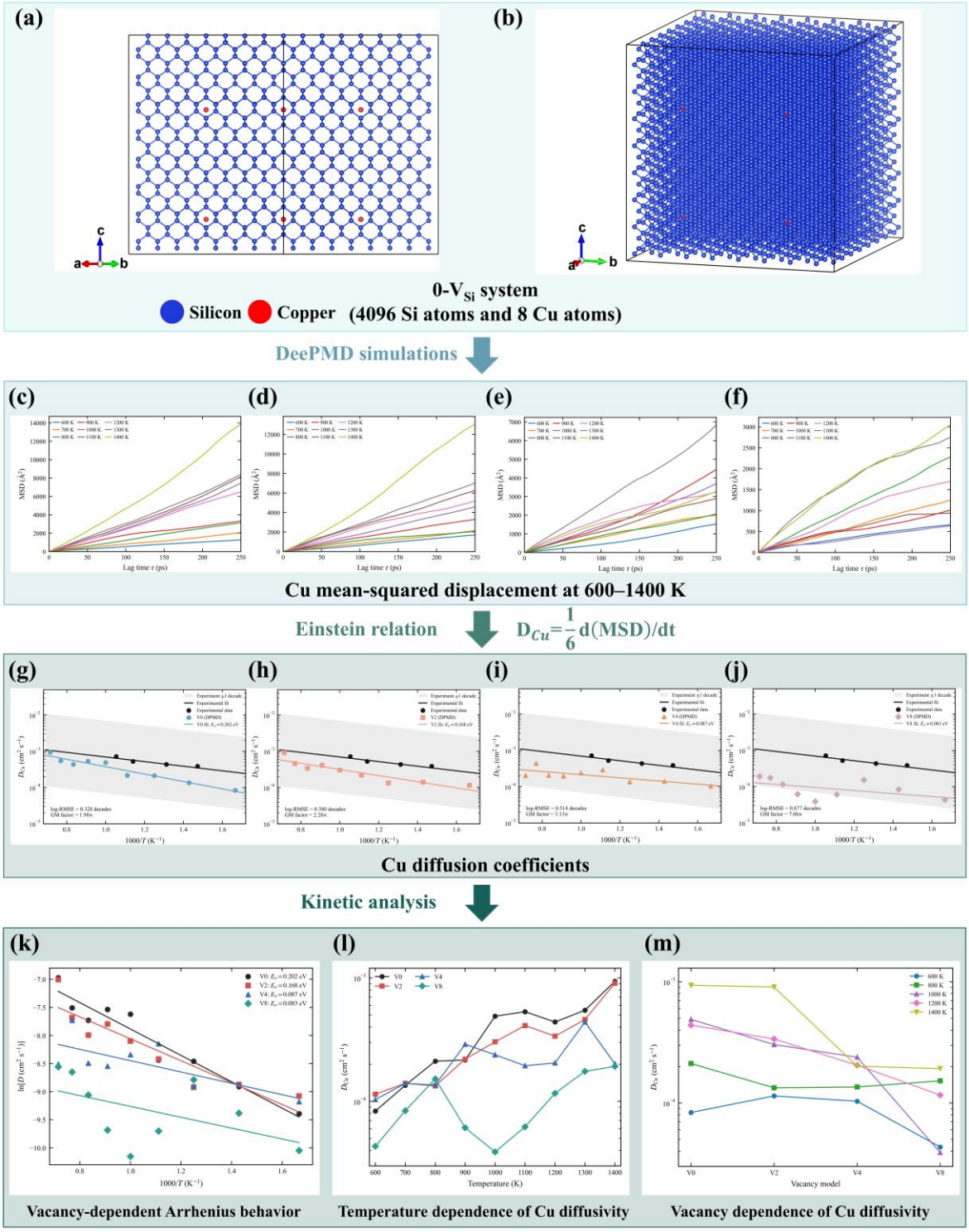



**Fig. 4 | Vacancy-dependent diffusion of Cu in crystalline Si. a,b,** Projected and three-dimensional views of the vacancy-free simulation cell containing 4096 Si atoms and eight Cu atoms. **c–f,** Ensemble-averaged

Cu MSDs between 600 and 1400 K for systems containing 0, 2, 4 and 8 Si vacancies, respectively. **g–j,** Arrhenius plots comparing the diffusion coefficients obtained for V0, V2, V4 and V8 with the intrinsic experimental reference. Grey regions indicate a factor-of-ten interval around the experimental relation. **k,** Combined Arrhenius representation for the four vacancy models. **l,** Temperature dependence of the calculated Cu diffusion coefficients. **m,** Cu diffusivity as a function of vacancy number at selected temperatures.

The Cu self-mean-squared displacement (MSD) was calculated from unwrapped trajectories while preserving individual atom identities. Averaging over the eight Cu atoms and available time origins gives the population-level MSDs in **Fig. 4c–f**. The same curves are shown at larger scale in Supplementary **Fig. S8a–d**, allowing their temperature dependence to be inspected for each vacancy model. Their long-lag-time slopes define the effective three-dimensional diffusion coefficients, $\boldsymbol{D}_{\mathrm{eff}}=1/6\cdot \mathrm{d}\langle \Delta r^2 \rangle/\mathrm{d}t$.

In vacancy-free Si, the increasing extent of Cu motion from 600 to 1400 K is evident in both the MSDs (**Fig. 4c**) and individual trajectories (**Fig. 5a–c**). The V0 Arrhenius fit yields an activation energy of 0.202 eV with $R^2$=0.93 (**Fig. 4g, k**). This value differs by 0.022 eV from the experimentally measured intrinsic interstitial-Cu diffusion barrier of 0.18±0.02 eV [57]. and is also comparable in scale to the 0.15 eV activation energy used for the experimental reference curve in Fig. 4g [26]. These values arise from different experimental analyses and temperature regimes and should not be treated as identical measurements. Nevertheless, their agreement in energy scale supports the ability of DeePMD to reproduce the temperature dependence of rapid interstitial-Cu transport. It complements the more direct migration-path benchmark in **Fig. 3a**, for which the DP and DFT barriers are 0.192 and 0.185 eV, respectively.

The trajectories reveal how vacancies modify that transport. In V2, spatially extended paths coexist with Cu atoms that spend prolonged periods within compact regions (**Fig. 5d–f**). This contrast becomes more pronounced in V4 (**Fig. 5g–i**) and V8 (**Fig. 5j–l**). The additional temperatures in Supplementary **Figs. S11–S34** show that the distinction between localized and extended paths occurs across the 36 model–temperature combinations, although neither every Cu atom nor every temperature follows a strictly monotonic trend. Such behaviour is consistent with competition between fast interstitial motion and vacancy-associated states. The vacancy-capture and Cu-complex pathways identified by the migration calculations in **Fig. 3** provide possible atomistic routes for this competition; the appearance of a compact trajectory alone, however, does not identify a particular defect complex.

We therefore evaluated vacancy association independently from the evolving atomic configurations. A Cu atom was classified as occupying a substitutional-like environment when it lay within 1.47 Å of a reconstructed Si site, or as vacancy-neighbouring when it lay within 2.82 Å of a reconstructed vacancy site. A three-frame median filter removed isolated changes in assignment. The fraction of Cu observations in either environment, averaged over the eight Cu atoms, sampled frames and nine temperatures, is approximately 0.1% for V0, 13.3% for V2, 31.7% for V4 and 56.7% for V8 (**Fig. S10a, b**). For V0, which contains no vacancy, the small assigned fraction refers only to substitutional-like environments. Representative atom-resolved state histories at 1000 K show that associated and unassociated periods can coexist within one simulation (**Fig. S10c**). These fractions quantify residence in environments defined by local structure; they do not imply that every associated Cu atom is permanently trapped. Several conditions

contain too few complete association–release events to determine reliable capture rates or residence-time distributions.

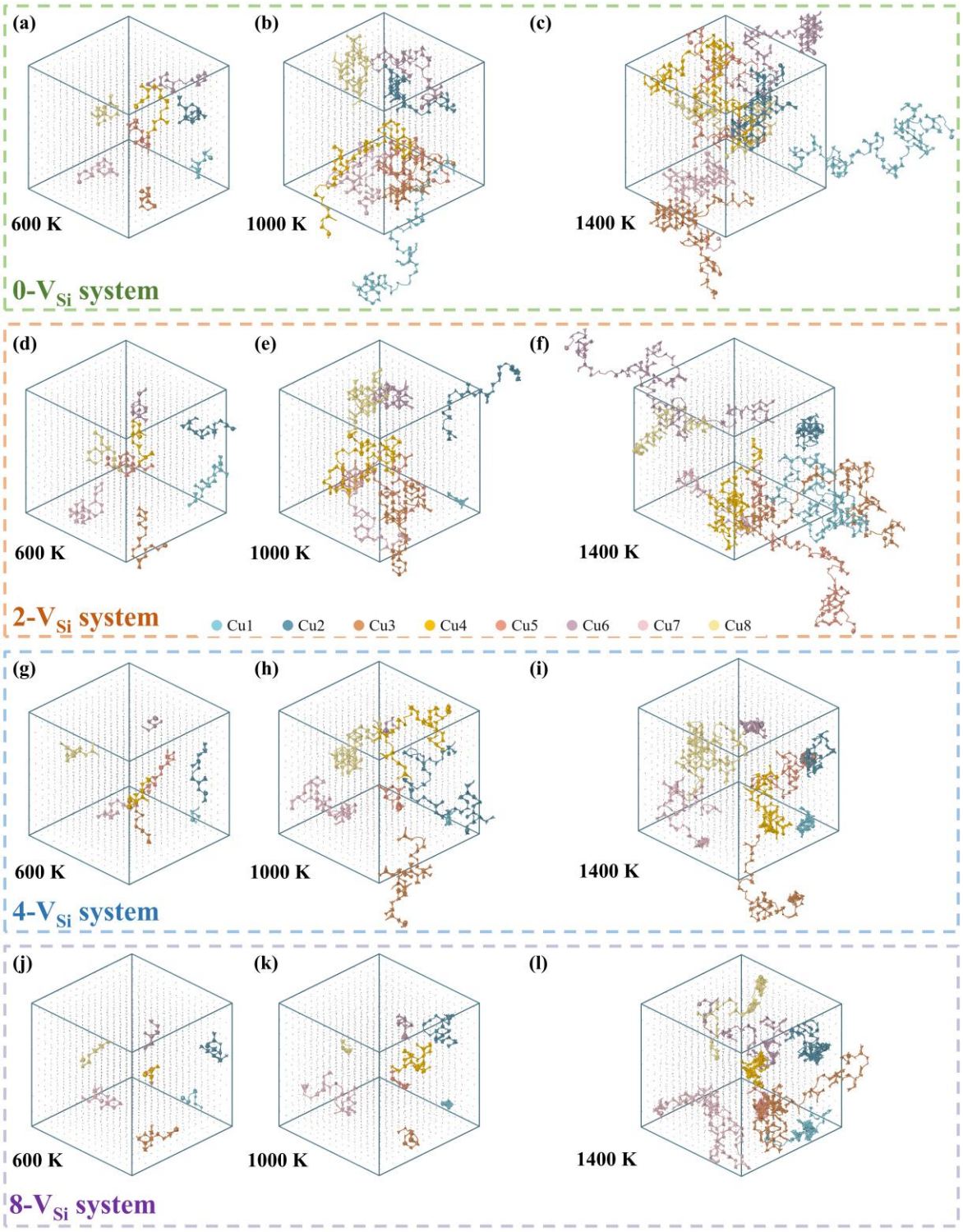



**Fig. 5 | Temperature- and vacancy-dependent Cu migration trajectories in crystalline Si. a–c,** V0; **d–f,** V2; **g–i,** V4; and **j–l,** V8 at 600, 1000 and 1400 K, respectively. The eight colors denote the unwrapped

trajectories of individual Cu atoms (Cu1–Cu8), while Si atoms are shown as grey points. All panels use the same projection and spatial scale.

Increasing vacancy-associated residence provides a physical explanation for the reduction of the **ensemble-averaged** MSD in vacancy-rich models (**Fig. 4d–f**). At a given temperature, Cu atoms making extended excursions continue to contribute strongly to the average, whereas atoms remaining near vacancy-associated sites contribute much less. The extracted $D_{\mathrm{eff}}$ therefore measures net spreading of the eight-atom population over the simulated interval, rather than the intrinsic mobility of its interstitial subset. The temperature and vacancy dependencies in **Fig. 4l, m** broadly reflect this suppression, while their deviations from strict monotonicity are consistent with the heterogeneous trajectories and limited number of Cu atoms sampled in each cell.

The Arrhenius plots reveal a progressive change in the ensemble transport response as the number of Si vacancies increases (**Fig. 4g–k**). Fits to the nine temperatures give apparent activation energies of 0.202, 0.168, 0.087 and 0.083 eV for V0, V2, V4 and V8, respectively, while the corresponding $R^2$ values decrease from 0.93 and 0.85 to 0.56 and 0.27. The temperature-dependent coefficients (**Fig. 4l**) and their values at selected vacancy concentrations (**Fig. 4m**) show an overall suppression of Cu spreading, although the trend is not monotonic at every temperature. The individual trajectories provide the microscopic context: extended Cu paths coexist with spatially confined motion, and this contrast becomes more pronounced in the vacancy-rich systems (**Fig. 5** and Supplementary **Figs. S11–S34**). Consistently, the structurally defined vacancy-associated Cu fraction increases across V0–V8 (**Fig. S10**). Thus, the measured MSD slope increasingly averages over Cu atoms with different residence histories and mobilities. The declining $R^2$ indicates that a single Arrhenius law becomes a poor description of this heterogeneous population, particularly for V4 and V8. Their fitted energies are therefore apparent, observation-window-dependent parameters, not evidence that vacancy capture lowers the barrier for an individual interstitial Cu hop.

### 2.5. Implantation and annealing reshape Cu depth profiles

**Figure 4 and 5** establish how temperature and Si vacancies influence Cu motion in crystalline Si. An implanted sample presents an additional challenge: Cu begins annealing from a strongly non-uniform depth distribution within a lattice altered by implantation. A diffusion coefficient alone cannot specify the ensuing concentration profile without this initial Cu distribution and defect landscape. We therefore test whether the atomistic description also reproduces an experimentally measurable outcome by comparing simulated profiles with secondary-ion mass spectrometry (SIMS) before and after annealing (**Fig. 6**). DFT–MD supplies the as-implanted configuration, which serves as the starting point for the subsequent DP-based annealing simulations.

For 70 keV Cu implantation, SIMS shows a broad concentration maximum several hundred angstroms below the surface and a measurable tail extending towards 900 Å (**Fig. 6a**). The DFT–MD implantation profile follows both regions more closely than the MC/BCA result. Its NRMSE is 0.114 over the full depth range, compared with 0.283 for MC/BCA (**Table 3**). The corresponding values are 0.118 versus 0.243 in the near-surface region (0–200 Å) and 0.115 versus 0.260 in the tail (700–900 Å). These differences arise

before the annealing calculations. They indicate that the quality of the implantation-derived initial condition contributes to the accuracy of the final profile; disagreement after annealing cannot be attributed solely to the diffusion model.

Annealing progressively changes the shape of the implanted distribution. At 773 K, the initial concentration maximum gives way to an extended high-concentration region, followed by a decrease at greater depth (**Fig. 6b**). At 1023 and 1073 K, the profile becomes flatter and its maximum decreases (**Fig. 6c, e**). **Fig. 6d, f** shows the same 1023 and 1073 K data, respectively, over reduced concentration ranges to make differences among SIMS and the two calculations easier to resolve. Across 0–900 Å, the DFT–MD+DP NRMSE values are 0.111, 0.113 and 0.118 at 773, 1023 and 1073 K, compared with 0.283, 0.257 and 0.223 for MC/BCA+KMC (**Table 3**). Thus, the coupled atomistic approach yields approximately 61%, 56% and 47% lower full-profile errors at these temperatures.

**Table 3**
The NRMSE for 70 keV Cu implanted into Si calculated using DFT-MD+DP method and MC/BCA+KMC method.

| Process | Method | NRMSE | | |
|---|---|---|---|---|
| | | Depth (0-900 Å) | Depth (0-200 Å) | Depth (700-900 Å) |
| Implantation | DFT-MD+DP | **0.114** | **0.118** | **0.115** |
| | MC/BCA+KMC | 0.283 | 0.243 | 0.260 |
| Annealing (773 K) | DFT-MD+DP | **0.111** | **0.117** | **0.107** |
| | MC/BCA+KMC | 0.283 | 0.241 | 0.273 |
| Annealing (1023 K) | DFT-MD+DP | **0.113** | **0.140** | **0.109** |
| | MC/BCA+KMC | 0.257 | 0.257 | 0.243 |
| Annealing (1073 K) | DFT-MD+DP | **0.118** | **0.147** | **0.103** |
| | MC/BCA+KMC | 0.223 | 0.302 | 0.218 |

Regional analysis shows that this improvement is not limited to the high-concentration part of the profile. Across the as-implanted and three annealed states, the DFT–MD+DP NRMSE ranges from 0.118 to 0.147 in the top region, compared with 0.241–0.302 for MC/BCA+KMC. In the tail, the corresponding ranges are 0.103–0.115 and 0.218–0.273 (**Table 3**). Because linear-space errors are more sensitive to large absolute concentration differences, we also examined the tail in log space: its residual is 0.046–0.056 dex for DFT–MD+DP and 0.117–0.138 dex for MC/BCA+KMC. The agreement in both measures supports a more faithful description of the lower-concentration tail, rather than an improvement confined to the profile maximum. Neither calculation is exact: the DFT–MD+DP profiles retain approximately 90% of the SIMS-integrated Cu amount in the 700–900 Å region, whereas the MC/BCA+KMC profiles retain approximately 73–79%.

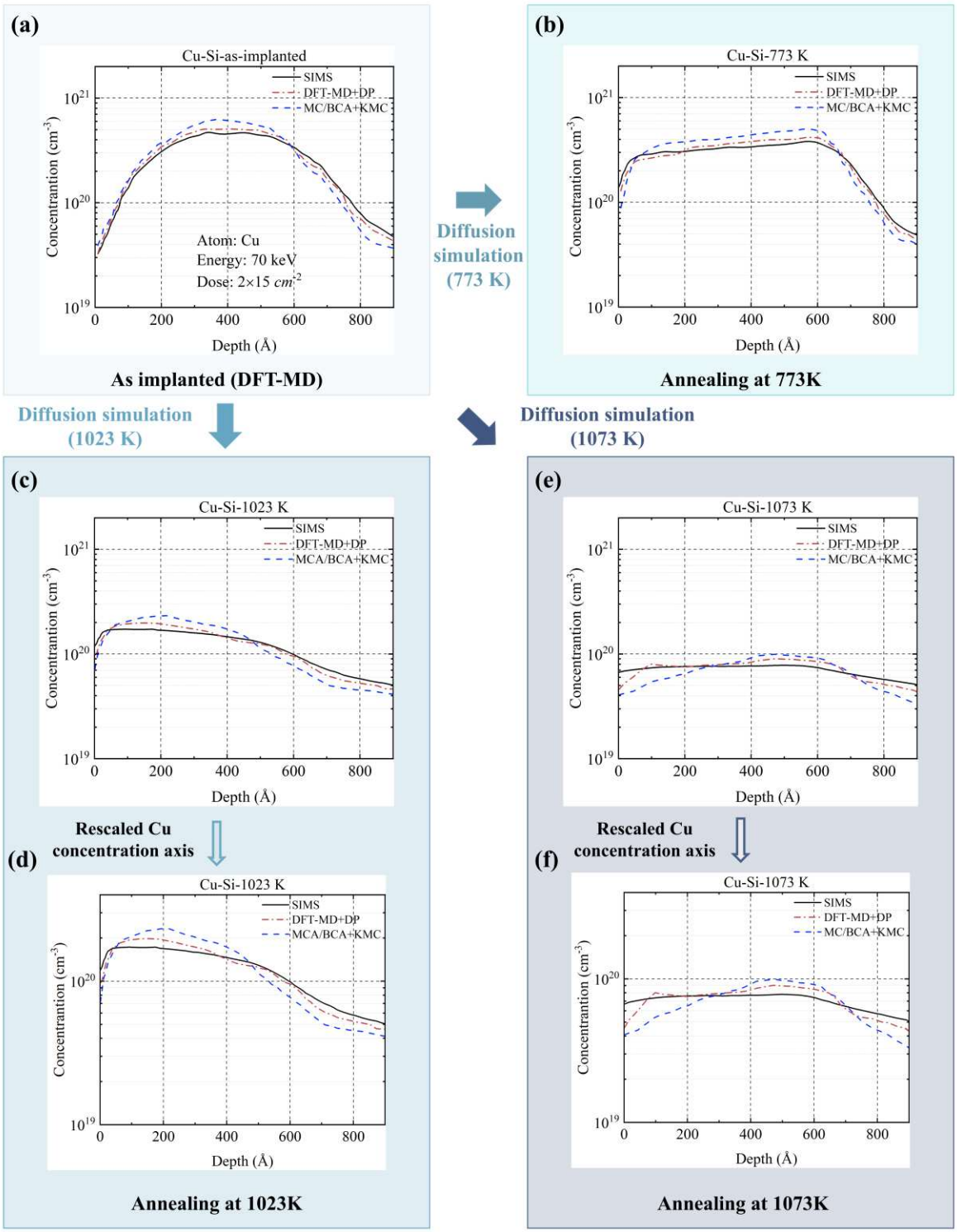



**Fig. 6 | Evolution of implanted Cu depth profiles during annealing.** Cu concentration profiles obtained by secondary-ion mass spectrometry (SIMS), the combined DFT–MD/DP approach and MC/BCA+KMC simulations are compared for the as-implanted state (a) and after annealing at 773 K (b), 1023 K (c, d) and 1073 K (e, f). Panels d and f reproduce the data in c and e, respectively, using reduced concentration ranges to highlight differences between the calculated and experimental profiles. The simulations reproduce the

temperature-dependent redistribution and broadening of the implanted Cu profile, including the near-surface and low-concentration tail regions.

The two depth regions probe different combinations of processes. The near-surface concentration depends on the initial implantation distribution and may also respond to defect evolution and boundary sinks during annealing; it should not be read as a measure of bulk diffusivity alone. The tail is particularly sensitive to Cu capable of migrating away from the implanted region, together with the defects that interrupt or retain that motion. The fast interstitial migration and vacancy-associated residence identified in **Fig. 2, 4** and **5** provide an atomistic basis for interpreting this competition, but agreement with a depth profile does not, by itself, identify a unique trapping rate or surface-loss pathway. The result is instead a consistent link between implantation, the evolving Cu–defect environment and the measured redistribution. This cross-stage perspective builds on the earlier oxygen-in-Si [45] and B-in-Si [44] DFT–MD+DP studies, while retaining the distinct Cu mechanism: rapid interstitial migration modified by vacancy association, rather than the interstitial-assisted kick-out process governing B.

## 3. Conclusion

We have developed an active-learning deep potential (DP) framework that links the elementary migration of Cu in Si to vacancy-dependent transport and the evolution of implanted Cu profiles. The model reproduces DFT energies and forces for representative Cu–Si environments and closely follows DFT minimum-energy paths for four interstitial-migration and vacancy-associated processes. For migration between neighbouring tetrahedral interstitial sites, the DP and DFT barriers are 0.192 and 0.185 eV, respectively. This agreement enables DeePMD simulations of systems containing approximately 4,000 Si atoms and eight Cu atoms—large enough to examine how multiple Cu atoms encounter different local defect environments within the same trajectory.

These simulations show why a single migration barrier cannot, by itself, describe Cu transport in vacancy-containing Si. Interstitial Cu can remain mobile, whereas Cu associated with a vacancy may spend substantial time in a locally confined or substitutional-like environment. Structural analysis finds that the fraction of Cu observations assigned to vacancy-associated or substitutional-like states rises from approximately 0.1% in V0 to 13%, 32% and 57% in V2, V4 and V8, respectively. Consistent with this growing heterogeneity, the apparent Arrhenius activation energies decrease from 0.202 to 0.168, 0.087 and 0.083 eV, while the corresponding fit quality deteriorates. The lower apparent energies in the vacancy-rich systems therefore should not be taken as evidence that vacancies lower the barrier of an individual Cu hop. Rather, the ensemble-averaged diffusivity reflects a temperature-dependent mixture of mobile and locally confined Cu, whose relative populations and residence times change during observation. Longer simulations that resolve repeated capture and release events are needed to quantify those kinetics.

The same atomistic framework improves the prediction of process-relevant Cu distributions. Coupling the implantation calculation to DP-based annealing gives full-depth-profile NRMSE values of 0.111–0.118 against SIMS, compared with 0.223–0.283 for the MC/BCA+KMC workflow assessed here; the advantage persists in the near-surface and low-concentration tail regions. Conventional MC/BCA+KMC remains valuable for rapid, long-timescale process simulation, but its prescribed collision physics and

kinetic-event catalogue can make evolving defect configurations and correlated Cu–vacancy interactions difficult to represent. The present comparison benchmarks these particular workflows, rather than establishing a limitation of every possible KMC model. DeePMD contributes a complementary capability: it follows many interacting atoms while retaining the DFT-validated local energetics needed to connect defect structure, Cu motion and the resulting concentration profile.

For Si processing, the results identify vacancy populations and their evolution during annealing as important controls on Cu redistribution, alongside temperature and the initial implanted profile. Vacancy association can suppress the mobile Cu population, but retaining Cu in defects is not necessarily benign: subsequent thermal treatment may release it and alter the near-surface concentration or deep tail. The framework can thus help screen implantation and annealing conditions against both forms of contamination, with SIMS providing the necessary profile-level validation. More broadly, whereas related atomistic frameworks have addressed oxygen redistribution and self-interstitial-mediated boron transport, the Cu–Si system illustrates how vacancy association produces distinct, spatially heterogeneous impurity dynamics. Resolving these dynamics at scales beyond routine AIMD is the principal physical advantage of large-scale DeePMD, and a basis for more reliable, defect-aware models of semiconductor processing.

## 4. Methods

### 4.1. Density Functional Theory Calculations

In this study, all Density Functional Theory (DFT) calculations were conducted using CP2K (version 8.1) software [58]. Double-zeta plus polarization (DZVP) basis sets were employed, combined with Goedecker-type pseudopotentials and the Perdew-Burke-Ernzerhof (PBE) exchange-correlation functional [59]. The energy cutoff was defined as 300 Ry, with the energy convergence threshold defined as $1.0\times10^{-6}$ Hartree. Monkhorst-Pack *k*-point gird with a 2×2×2 grid was used for the Brillouin zone. Lattice relaxation was performed with a force convergence criterion of $2.0\times10^{-4}$ Hartree/Bohr (about 10 meV/Å). For NEB calculations, we employed a force convergence criterion of $2.0 \times 10^{-4}$ Hartree/Bohr (about 10 meV/Å) to relax the intermediate images.

### 4.2. Deep Potential Molecular Dynamics Simulations

The initial system was consisted of 4104 atoms (4096 Si atoms and 8 Cu atoms), with dimensions of 43.5×43.5×43.5 $Å^3$, as shown in **Fig. 4a, b**. For the diffusion calculations, DeePMD simulations were performed using the deepmd-kit [60] within the LAMMPS package [61]. We enforced periodic boundary conditions along the *x*, *y* and *z* directions. Throughout the simulations, the canonical (NVT) ensemble was utilized with a Nose-Hoover thermostat [62,63]. The time step is set to 1 fs and 500 ps of DeePMD simulations were conducted at high temperatures (>600 K).

## Data Availability

Data supporting the key findings of this study are provided within the article and Supplementary Information files. Raw data generated during this study are available from the corresponding authors upon request.

## Acknowledgement

This work is supported by the China Postdoctoral Science Foundation under Grant Number 2026M793784 and the Macau Young Scholars Program under Grant Number AM2026011. And we are grateful for resources from High Performance Computing Center of Central South University.

## Author Contributions

J.S.C. and M.Z.L conceived the idea for the project. J.S.C. carried out the DFT, DeePMD, AIMD and CMD simulations. J.S.C. trained and tested the DP model. J.S.C. and M.Z.L wrote the paper. Y.W.S. and X.Z.W. revised and proofed the paper. All authors discussed the results and commented on the manuscript. The project was supported by the funding of J.S.C.

## Competing Interests

The authors declare no competing interests.

## References


1 Gambino, J. P., Adderly, S. A. & Knickerbocker, J. U. An overview of through-silicon-via technology and manufacturing challenges. *Microelectronic Engineering* **135**, 73–106 (2015).

2 Datta, M. Applications of electrochemical microfabrication: An introduction. *IBM Journal of research and development* **42**, 563–566 (1998).

3 Bea, J., Lee, K., Fukushima, T., Tanaka, T. & Koyanagi, M. Evaluation of Cu diffusion from Cu through-silicon via (TSV) in three-dimensional LSI by transient capacitance measurement. *IEEE Electron Device Letters* **32**, 940–942 (2011).

4 Istratov, A., Flink, C., Hieslmair, H., McHugo, S. & Weber, E. Diffusion, solubility and gettering of copper in silicon. *Materials Science and Engineering: B* **72**, 99–104 (2000).

5 Istratov, A. A. & Weber, E. R. Physics of copper in silicon. *Journal of The Electrochemical Society* **149**, G21–G30 (2002).

6 Mehta, R., Chugh, S. & Chen, Z. Transfer-free multi-layer graphene as a diffusion barrier. *Nanoscale* **9**, 1827–1833 (2017).

7 Zhao, Y. & Lu, G. First-principles simulations of copper diffusion in tantalum and tantalum nitride. *Physical Review B—Condensed Matter and Materials Physics* **79**, 214104 (2009).

8 Graff, K. *Metal impurities in silicon-device fabrication*. (Springer Science & Business Media, 2013).

9 Goetzberger, A. & Shockley, W. Metal precipitates in silicon p-n junctions. *Journal of Applied Physics* **31**, 1821–1824 (1960).

10 Busta, H. & Waggener, H. Precipitation-induced currents and generation-recombination currents in intentionally contaminated silicon p+ n junctions. *Journal of The Electrochemical Society* **124**, 1424–1429 (1977).

11 Böhm, R. & Klose, H. Copper in silicon n+-p junctions. *physica status solidi (a)* **9**, K165–K168 (1972).

12 Beeler, F., Andersen, O. & Scheffler, M. Electronic and magnetic structure of 3d–transition-metal point defects in silicon calculated from first principles. *Physical Review B* **41**, 1603 (1990).

13 Hamaker, R., Putney, Z., Ayers, R. & Smith, P. Degradation mechanism for silicon p+-n junctions under forward bias. *Solid-State Electronics* **24**, 1001–1008 (1981).

14 Honda, K., Ohsawa, A. & Toyokura, N. Breakdown in silicon oxides—correlation with Cu precipitates. *Applied physics letters* **45**, 270–271 (1984).

15 Hiramoto, K., Sano, M., Sadamitsu, S. & Fujino, N. Degradation of gate oxide integrity by metal impurities. *Japanese journal of applied physics* **28**, L2109 (1989).

16 Miyazaki, M., Sano, M., Shigeo Sumita, S. S. & Nobukatsu Fujino, N. F. Influence of metal impurities on leakage current of Si N+ P diode. *Japanese journal of applied physics* **30**, L295 (1991).

17 Davis, J. R. *et al.* Impurities in silicon solar cells. *IEEE Transactions on electron devices* **27**, 677–687 (1980).

18 Hopkins, R. & Rohatgi, A. Impurity effects in silicon for high efficiency solar cells. *Journal of*

*Crystal Growth* **75**, 67–79 (1986).

19 Prigge, H., Gerlach, P., Hahn, P. O., Schnegg, A. & Jacob, H. Acceptor compensation in silicon induced by chemomechanical polishing. *Journal of The Electrochemical Society* **138**, 1385–1389 (1991).

20 Naito, S. & Nakashizu, T. Electric degradation and defect formation of silicon due to Cu, Fe, and Ni contamination. *MRS Online Proceedings Library (OPL)* **262**, 641 (1992).

21 Itsumi, M., Sato, Y., Imai, K. & Yabumoto, N. Characterization of metallic impurities in Si using a recombination-lifetime correlation method. *Journal of applied physics* **82**, 3250–3255 (1997).

22 Rotondaro, A. *et al.* Impact of Fe and Cu contamination on the minority carrier lifetime of silicon substrates. *Journal of the Electrochemical Society* **143**, 3014–3019 (1996).

23 Henley, W. B., Ramappa, D. A. & Jastrezbski, L. Detection of copper contamination in silicon by surface photovoltage diffusion length measurements. *Applied physics letters* **74**, 278–280 (1999).

24 Gaspar, G. *et al.* Influence of copper diffusion on lifetime degradation in n-type Czochralski silicon for solar cells. *Energy Procedia* **77**, 586–591 (2015).

25 Frank, W. in *Crucial Issues in Semiconductor Materials and Processing Technologies* 383–402 (Springer, 1992).

26 Istratov, A. A., Flink, C., Hieslmair, H., Weber, E. R. & Heiser, T. Intrinsic diffusion coefficient of interstitial copper in silicon. *Physical review letters* **81**, 1243 (1998).

27 Bracht, H. Copper related diffusion phenomena in germanium and silicon. *Materials science in semiconductor processing* **7**, 113–124 (2004).

28 Shirai, K., Michikita, T. & Katayama-Yoshida, H. Molecular dynamics study of fast diffusion of Cu in silicon. *Japanese journal of applied physics* **44**, 7760 (2005).

29 Sharan, A., Gui, Z. & Janotti, A. Hybrid-functional calculations of the copper impurity in silicon. *Physical Review Applied* **8**, 024023 (2017).

30 Matsukawa, K., Shirai, K., Yamaguchi, H. & Katayama-Yoshida, H. Diffusion of transition-metal impurities in silicon. *Physica B: Condensed Matter* **401**, 151–154 (2007).

31 Yamaguchi, H., Shirai, K. & Katayama-Yoshida, H. The Stable Site and Diffusion of Impurity Cu in Si. *J. Comput. Theor. Nanosci* **6**, 2619 (2009).

32 Estreicher, S. K. First-principles theory of copper in silicon. *Materials science in semiconductor processing* **7**, 101–111 (2004).

33 Wahl, U., Vantomme, A., Langouche, G., Correia, J. & collaboration, I. Lattice location and stability of ion implanted Cu in Si. *Physical Review Letters* **84**, 1495 (2000).

34 Estreicher, S. & Hastings, J. Cu-related complexes in silicon. *Materials Science and Engineering: B* **58**, 155–158 (1999).

35 Estreicher, S., West, D., Pruneda, J., Knack, S. & Weber, J. Formation and properties of three copper pairs in silicon. *MRS Online Proceedings Library* **719**, 139 (2001).

36 Estreicher, S., West, D., Goss, J., Knack, S. & Weber, J. First-principles calculations of pseudolocal vibrational modes: the case of Cu and Cu pairs in Si. *Physical review letters* **90**, 035504 (2003).

37 Fujita, N., Jones, R., Öberg, S., Briddon, P. R. & Blumenau, A. A theoretical study of copper

contaminated dislocations in silicon. *Solid State Phenomena* **131**, 259–264 (2008).

38 Mizushima, Y., Kim, Y., Nakamura, T., Uedono, A. & Ohba, T. Behavior of copper contamination on backside damage for ultra-thin silicon three dimensional stacking structure. *Microelectronic Engineering* **167**, 23–31 (2017).

39 Chen, P. *et al.* First-principles study of copper contamination in silicon semiconductor. *Surfaces and Interfaces* **31**, 102084 (2022).

40 Akbari Roshan, K., Khajeh Talkhoncheh, M., Mueller, J. E., Goddard III, W. A. & van Duin, A. C. Development of the ReaxFF reactive force field for Cu/Si systems with application to copper cluster formation during Cu diffusion inside silicon. *The Journal of Physical Chemistry C* **125**, 19455–19466 (2021).

41 Ding, X. *et al.* Efficient and accurate atomistic modeling of dopant migration using deep neural network. *Materials Science in Semiconductor Processing* **143**, 106513 (2022).

42 Chen, J. *et al.* Improving the accuracy of ion implantation simulations through the use of DFT-MD methodology. *Physica B: Condensed Matter* **675**, 415616 (2024).

43 Chen, J. *et al.* Application of DP-MD methodology in ion implantation for wide bandgap power semiconductor materials. *Surfaces and Interfaces* **62**, 106140 (2025).

44 Chen, J. *et al.* Atomistic simulation of boron implantation and defect-mediated diffusion in silicon via DFT-MD and deep potential molecular dynamics. *Physical Chemistry Chemical Physics* (2026).

45 Yan, X. *et al.* Deep learning modeling of oxygen redistribution and thermal transport in silicon on insulator and buried oxide layers. *Communications Materials* **7**, 80 (2026). https://doi.org/10.1038/s43246-026-01130-z

46 Zhang, L., Han, J., Wang, H., Saidi, W. & Car, R. End-to-end symmetry preserving inter-atomic potential energy model for finite and extended systems. *Advances in neural information processing systems* **31** (2018).

47 Henkelman, G., Uberuaga, B. P. & Jónsson, H. A climbing image nudged elastic band method for finding saddle points and minimum energy paths. *The Journal of chemical physics* **113**, 9901–9904 (2000).

48 Henkelman, G. & Jónsson, H. Improved tangent estimate in the nudged elastic band method for finding minimum energy paths and saddle points. *The Journal of chemical physics* **113**, 9978–9985 (2000).

49 Sadigh, B. *et al.* Mechanism of boron diffusion in silicon: An ab initio and kinetic Monte Carlo study. *Physical review letters* **83**, 4341 (1999).

50 Lin, L., Kirichenko, T., Banerjee, S. K. & Hwang, G. S. Boron diffusion in strained Si: A first-principles study. *Journal of applied physics* **96**, 5543–5547 (2004).

51 Windl, W., Bunea, M., Stumpf, R., Dunham, S. & Masquelier, M. Ab-initio pseudopotential calculations of boron diffusion in silicon. *MRS Online Proceedings Library (OPL)* **568**, 91 (1999).

52 Wan, W., Zhang, Q., Cui, Y. & Wang, E. First principles study of lithium insertion in bulk silicon. *Journal of physics: Condensed matter* **22**, 415501 (2010).

53 Kyrtsos, A., Matsubara, M. & Bellotti, E. in *Journal of Physics: Conference Series.* 012143 (IOP Publishing).
54 Daw, M. S. & Baskes, M. I. Embedded-atom method: Derivation and application to impurities, surfaces, and other defects in metals. *Physical review B* **29**, 6443 (1984).
55 Tersoff, J. Modeling solid-state chemistry: Interatomic potentials for multicomponent systems. *Physical review B* **39**, 5566 (1989).
56 Plimpton, S. Fast parallel algorithms for short-range molecular dynamics. *Journal of computational physics* **117**, 1–19 (1995).
57 Keller, R. *et al.* Copper in silicon. *Physical review letters* **65**, 2023 (1990).
58 VandeVondele, J. *et al.* Quickstep: Fast and accurate density functional calculations using a mixed Gaussian and plane waves approach. *Computer Physics Communications* **167**, 103–128 (2005). https://doi.org/10.1016/j.cpc.2004.12.014
59 Perdew, J. P. B., Kieron; Ernzerhof, Matthias Generalized Gradient Approximation Made Simple. *Phys. Rev. Lett* **77**, 3865–3868 (1996).
60 Wang, H., Zhang, L., Han, J. & E, W. DeePMD-kit: A deep learning package for many-body potential energy representation and molecular dynamics. *Computer Physics Communications* **228**, 178–184 (2018). https://doi.org/10.1016/j.cpc.2018.03.016
61 Plimpton, S. Fast parallel algorithms for short-range molecular dynamics. **117**, 1–19 (1995).
62 Hoover, W. G. J. P. r. A. Canonical dynamics: Equilibrium phase-space distributions. **31**, 1695 (1985).
63 Nosé, S. J. T. J. o. c. p. A unified formulation of the constant temperature molecular dynamics methods. **81**, 511–519 (1984).

# Figures

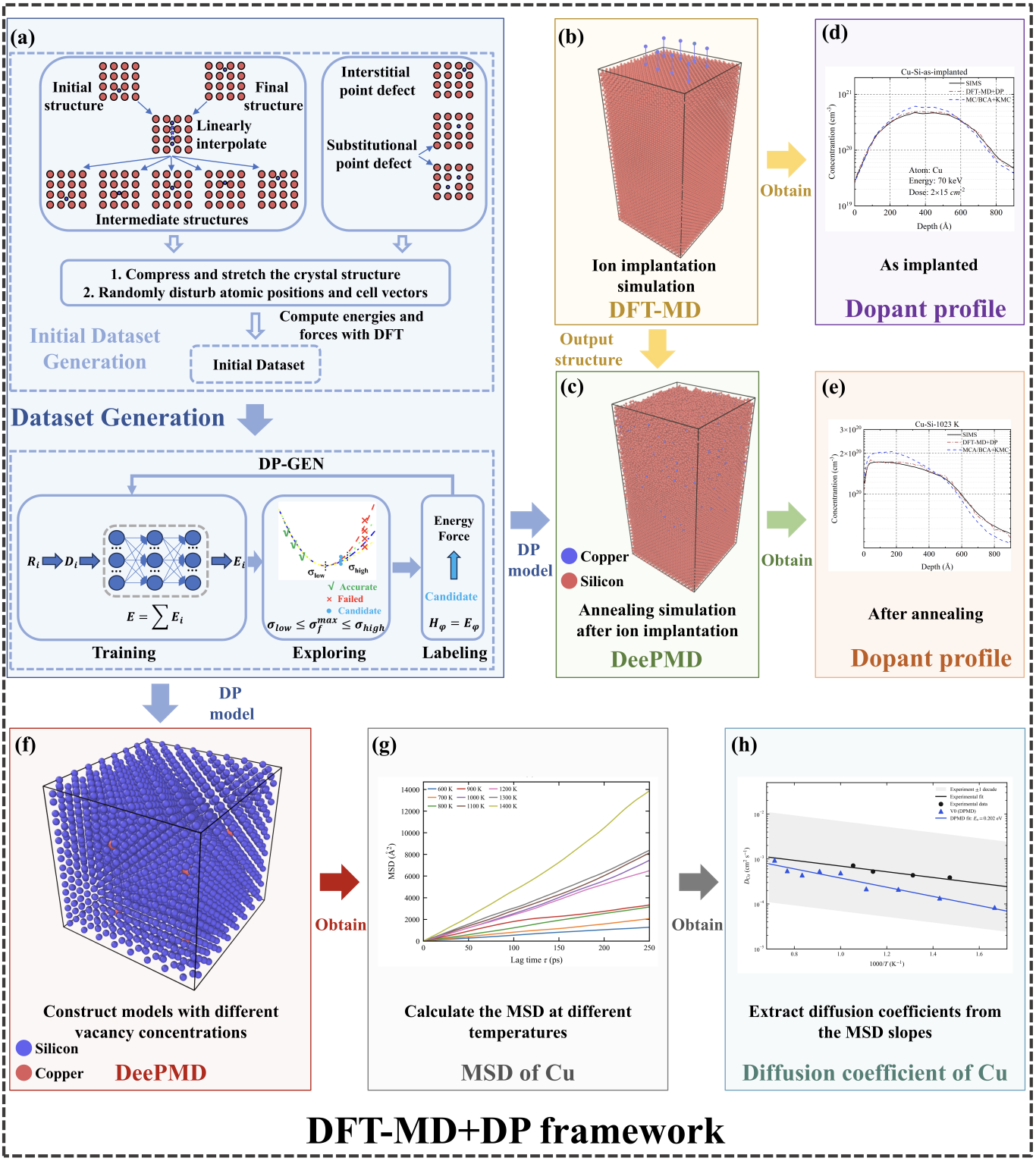



Figure 1

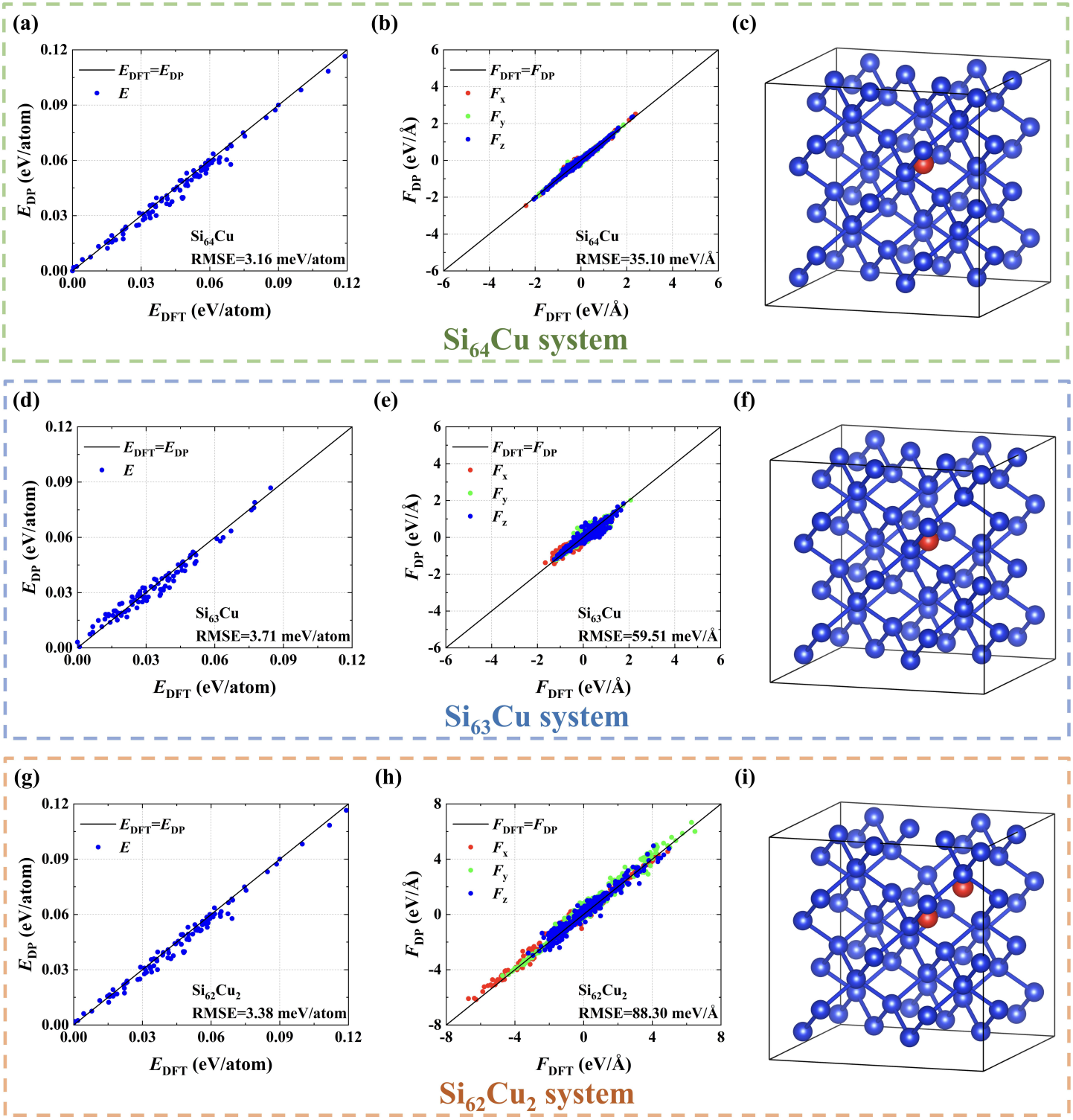

(a)
(b)
(c)
$E_{DFT}$=$E_{DP}$
E
$E_{DP}$ (eV/atom)
$E_{DFT}$ (eV/atom)
$Si_{64}Cu$
RMSE=3.16 meV/atom
$F_{DFT}$=$F_{DP}$
$F_x$
$F_y$
$F_z$
$F_{DP}$ (eV/Å)
$F_{DFT}$ (eV/Å)
$Si_{64}Cu$
RMSE=35.10 meV/Å
$Si_{64}Cu$ system
(d)
(e)
(f)
$Si_{63}Cu$
RMSE=3.71 meV/atom
RMSE=59.51 meV/Å
$Si_{63}Cu$ system
(g)
(h)
(i)
$Si_{62}Cu_2$
RMSE=3.38 meV/atom
RMSE=88.30 meV/Å
$Si_{62}Cu_2$ system

Figure 2

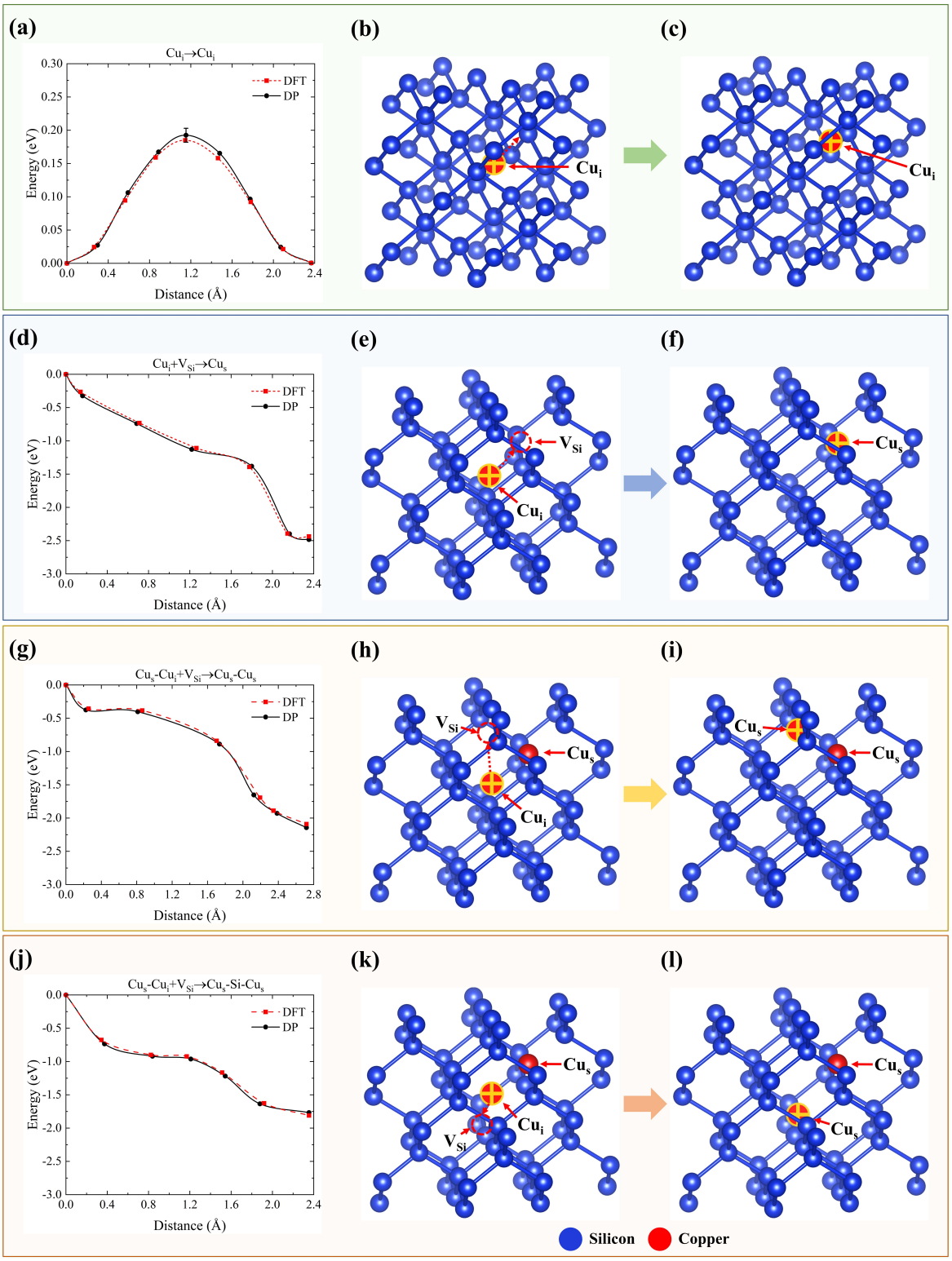

(a)
(b)
(c)
Cu$_i$→Cu$_i$
DFT
DP
Energy (eV)
Distance (Å)
Cu$_i$
Cu$_i$
(d)
(e)
(f)
Cu$_i$+V$_{Si}$→Cu$_s$
V$_{Si}$
Cu$_i$
Cu$_s$
(g)
(h)
(i)
Cu$_s$-Cu$_i$+V$_{Si}$→Cu$_s$-Cu$_s$
V$_{Si}$
Cu$_s$
Cu$_i$
Cu$_s$
Cu$_s$
(j)
(k)
(l)
Cu$_s$-Cu$_i$+V$_{Si}$→Cu$_s$-Si-Cu$_s$
Cu$_s$
Cu$_i$
V$_{Si}$
Cu$_s$
Cu$_s$
Silicon
Copper

Figure 3

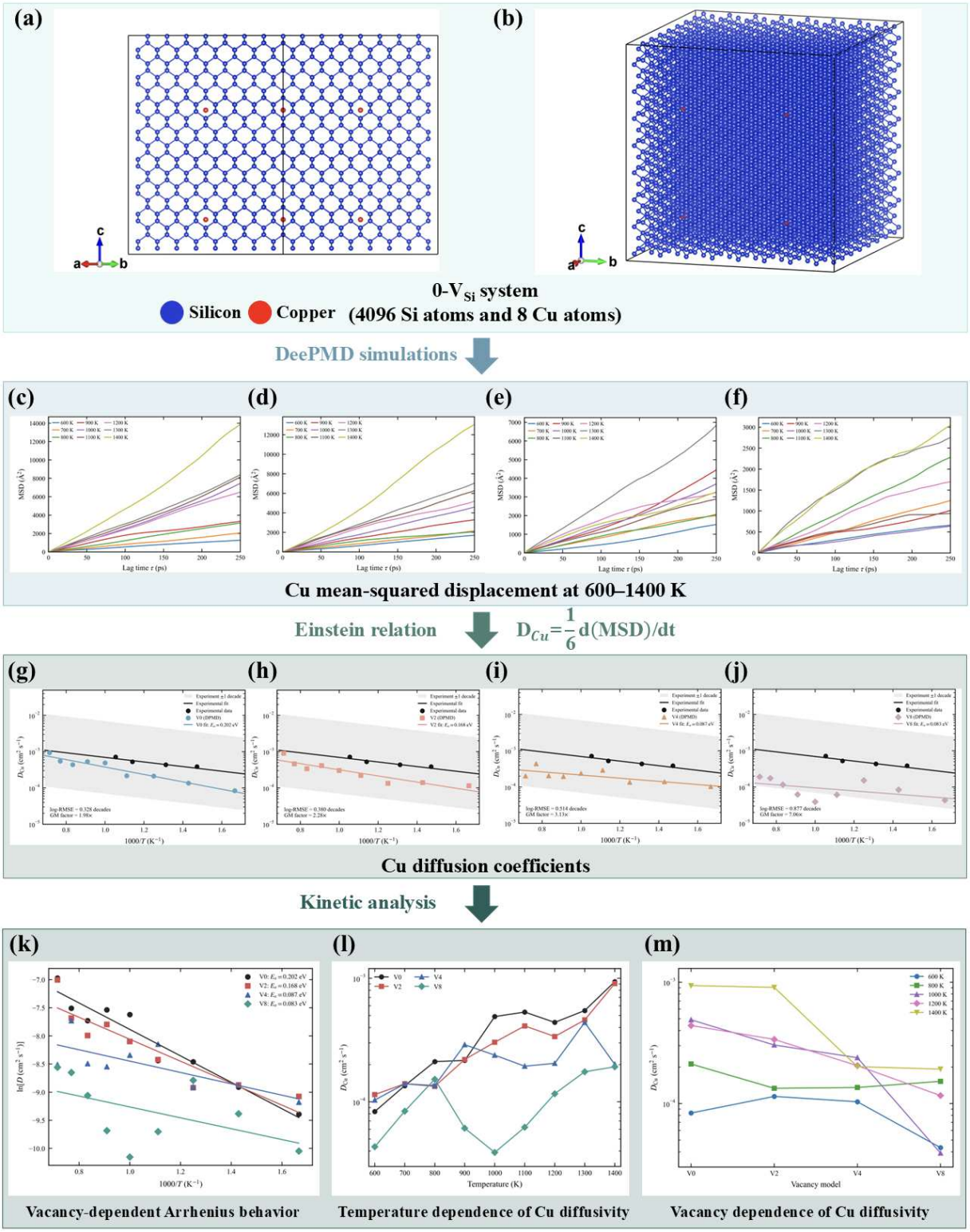

(a)
(b)
c
a
b
0-$V_{Si}$ system
Silicon
Copper
(4096 Si atoms and 8 Cu atoms)
DeePMD simulations
(c)
(d)
(e)
(f)
MSD (Å²)
Lag time τ (ps)
Cu mean-squared displacement at 600–1400 K
Einstein relation
$D_{Cu}=\frac{1}{6}d(MSD)/dt$
(g)
(h)
(i)
(j)
$D_{Cu}$ (cm² s⁻¹)
1000/T (K⁻¹)
Cu diffusion coefficients
Kinetic analysis
(k)
(l)
(m)
ln(D (cm² s⁻¹))
Temperature (K)
Vacancy model
Vacancy-dependent Arrhenius behavior
Temperature dependence of Cu diffusivity
Vacancy dependence of Cu diffusivity

Figure 4

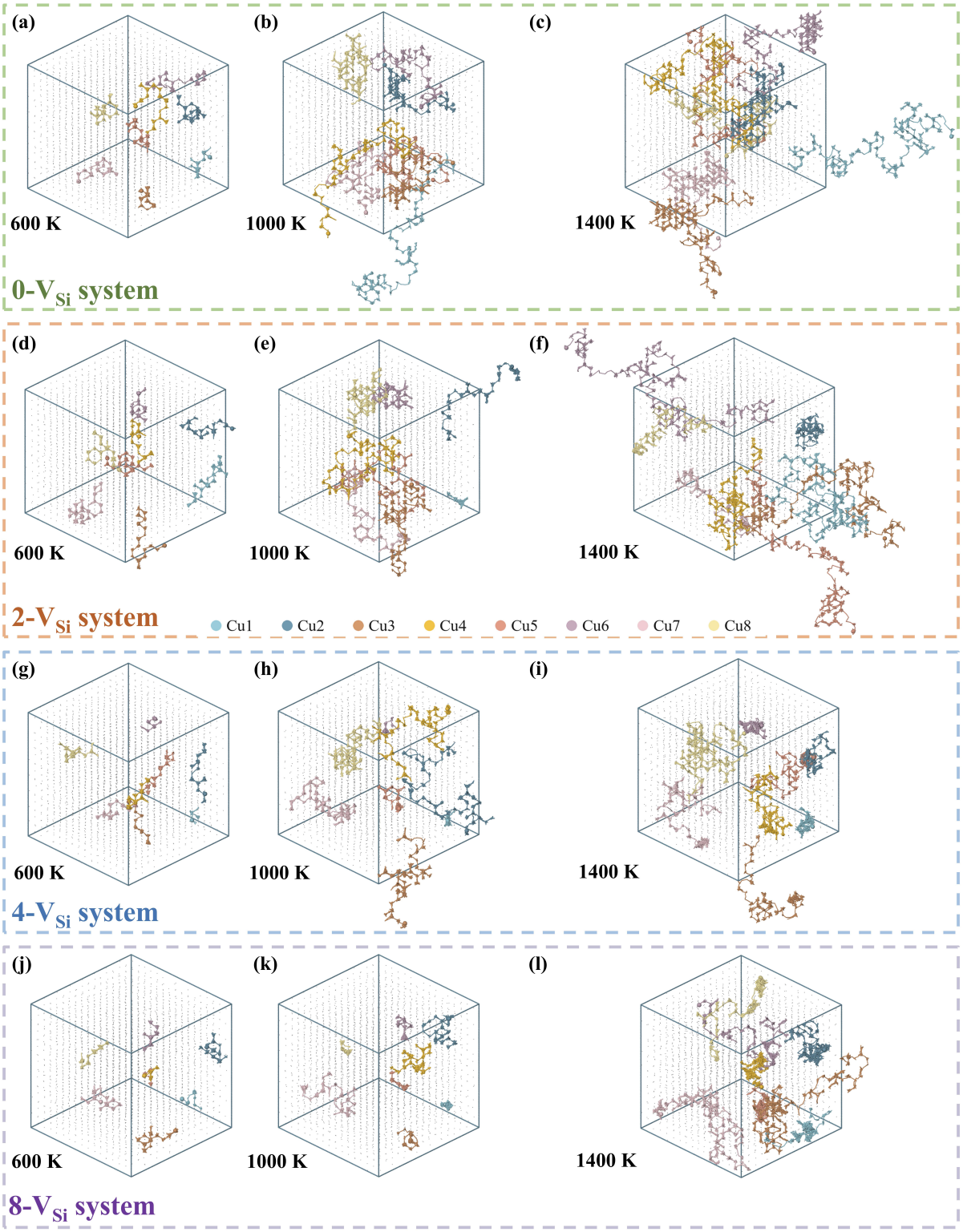

(a)
(b)
(c)
600 K
1000 K
1400 K
0-V$_{Si}$ system
(d)
(e)
(f)
600 K
1000 K
1400 K
2-V$_{Si}$ system
Cu1
Cu2
Cu3
Cu4
Cu5
Cu6
Cu7
Cu8
(g)
(h)
(i)
600 K
1000 K
1400 K
4-V$_{Si}$ system
(j)
(k)
(l)
600 K
1000 K
1400 K
8-V$_{Si}$ system

Figure 5

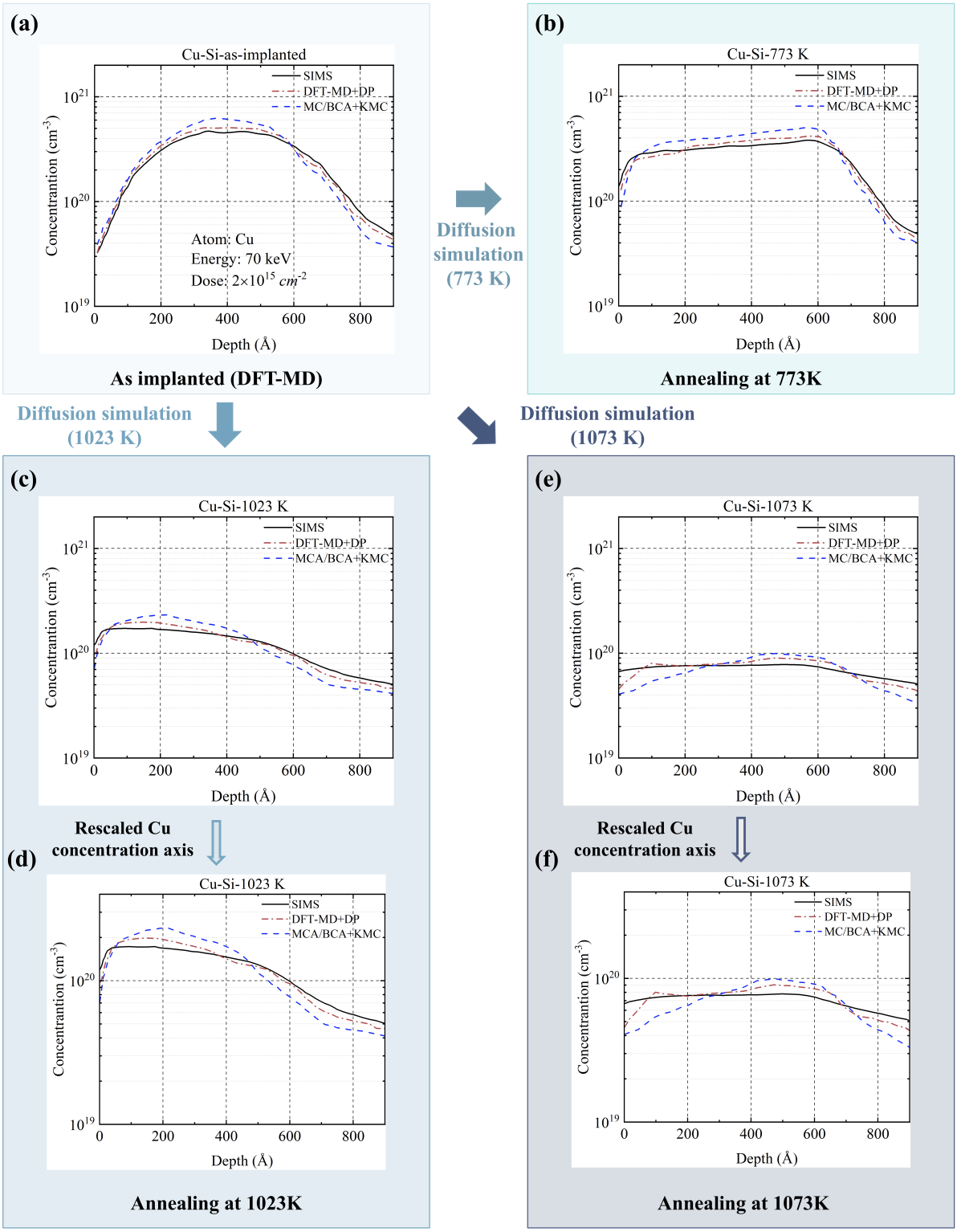



Figure 6

# Supplementary Files

This is a list of supplementary files associated with this preprint. Click to download.

- Supportinginformation.docx